Journal of Atmospheric and Solar–Terrestrial Physics 247 (2023) 106069

Contents lists available at ScienceDirect

Journal of Atmospheric and Solar–Terrestrial Physics

journal homepage: www.elsevier.com/locate/jastp

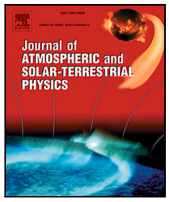

Research paper

A new index for statistical analyses and prediction of travelling ionospheric disturbances

Claudia Borries [a,*], Arthur Amaral Ferreira [a,b], Grzegorz Nykiel [c,d], Renato Alves Borges [b]

[a] German Aerospace Center, DLR, Institute for Solar-Terrestrial Phyisics, Neustrelitz, Germany
[b] University of Brasília, Department of Electrical Engineering, Brasília, Brazil
[c] Gdansk University of Technology, Faculty of Civil and Environmental Engineering, Gdansk, Poland
[d] Gdansk University of Technology, Digital Technologies Center, Gdansk, Poland

ARTICLE INFO

Keywords:
TIDs
Solar wind drivers
Geomagnetic storms
Prediction

ABSTRACT

Travelling Ionospheric Disturbances (TIDs) are signatures of atmospheric gravity waves (AGWs) observed in changes in the electron density. The analysis of TIDs is relevant for studying coupling processes in the thermosphere–ionosphere system. A new TID index A_{TID} is introduced, which is based on an easy extension of the commonly used approach for TID detection. This TID activity index, which can be applied for individual Global Navigation Satellite Systems (GNSS) stations and also for mapping TID activity, is capable to study both Large Scale TIDs (LSTIDs) and Medium Scale TIDs (MSTIDs).

A_{TID} is well applicable for statistical analyses and investigations of the source mechanisms of TIDs. Correlation studies presented here reveal that LSTID magnitudes at mid-latitudes are well correlated with solar wind derived parameters, like the Kan-Lee merging electric field (E_{KL}), the intermediate function (E_{WAV}) and the modified version of the Akasufo ϵ parameter (ϵ_3). Thus, the magnitude of the global solar-wind energy input into the Earth's magnetosphere–ionosphere–thermosphere system is most relevant for the LSTID generation. The correlation with common geomagnetic activity indices shows that also sudden changes in the magnetosphere–ionosphere–thermosphere system are relevant. Good correlation results are limited to mid-latitudes. High-latitude regions are impacted by auroral processes and low-latitude regions by coupling from below and other instabilities.

A_{TID} can be used for the modelling and prediction as demonstrated with a prediction model for storm induced LSTIDs, based on solar wind observations only. Very good performance of this LSTIDs prediction model in mid-latitudes has been proven.

1. Introduction

During geomagnetic storms, great amounts of energy are transferred from the solar wind into the Earth system, causing significant changes in the magnetosphere, ionosphere and thermosphere. In the auroral region electrojets and currents intensify very suddenly and the thermosphere heats up significantly due to the dissipation of the currents. This very sudden heating and expansion of the thermosphere generates large-scale Atmospheric Gravity Waves (AGWs), which develop at the equatorward boundary of the auroral oval and propagate equatorward (Borries et al., 2017). One of the best methods to study these large scale AGWs is the investigation of their signature in the ionosphere, the Large Scale Travelling Ionospheric Disturbances (LSTIDs). Measurements of the Total Electron Content (TEC), which can be well derived from ground based measurements of Global Navigation Satellite Systems (GNSS), are ideal to investigate the occurrence and wave properties of LSTIDs. In the past decades, many case studies and statistical investigations of LSTIDs during geomagnetic storms based on GNSS data have been published (e.g. Afraimovich et al., 2008; Ding et al., 2008; Borries et al., 2009; Habarulema et al., 2015; Tsugawa et al., 2004; Zakharenkova et al., 2016). Also the signatures of smaller scale waves, the Medium Scale TIDs (MSTIDs), can be observed with GNSS based TEC (e.g. Saito et al., 2007; Tsugawa et al., 2007; Hernández-Pajares et al., 2006). While LSTIDs are generated mainly due to the solar wind energy input and auroral heating, the MSTID are considered to be predominantly originating from atmospheric gravity waves coming from lower regions of the atmosphere. Investigations on the E-F region coupling also suggest that MSTIDs may also be generated by coupling between F-region and E-region instabilities, such as sporadic E-layer instabilities (Liu et al., 2019b; Sivakandan et al., 2022). The phenomenological investigation of Travelling Ionospheric

* Corresponding author.
E-mail address: claudia.borries@dlr.de (C. Borries).

https://doi.org/10.1016/j.jastp.2023.106069
Received 18 November 2022; Received in revised form 14 March 2023; Accepted 11 April 2023
Available online 22 April 2023

Disturbances (TIDs) progresses well, but modelling and forecasting of TIDs is still not sufficiently addressed.

MSTIDs impact the performance of positioning applications and during storms the large scale atmospheric gravity waves (travelling atmospheric disturbance) contribute to significant perturbations in the ionosphere (positive storms, c.f. Prölss, 2006). Therefore, forecasting the occurrence and amplitude of TIDs is required. Still, this is a pending task. Research projects like Tech-TIDE (Warning and Mitigation Technologies for Travelling Ionospheric Disturbances Effects, Belehaki et al., 2020) worked on the exact identification and tracking of TIDs with different scales. But, a precise forecast of TIDs, has not been established yet.

Numerous case studies and a number of statistical analyses of LSTIDs in different regions of the globe indicates that the generation and amplitudes of LSTIDs depend on geomagnetic activity. The occurrence rate of LSTIDs increases with increasing magnitude of kp, ap and AE and local auroral electrojet indices, as shown by Tsugawa et al. (2004) and Ding et al. (2008). A significant correlation of the magnitude of LSTIDs with the AE index has been demonstrated for F-region height enhancements by Hajkowicz (1991) and for TEC by Borries et al. (2009). In a case study, Cherniak and Zakharenkova (2018) observed that an increase of the Field Aligned Currents (FACs) magnitude led to a simultaneous intensification of the LSTIDs occurrence at high latitudes. A variety of studies show that the LSTID generation evidently depend on intense high-latitude electrodynamic processes driven by solar wind energy (e.g. Zakharenkova et al., 2016; Lyons et al., 2019). But, they do not give a clear indication, which geomagnetic parameter correlates best with the LSTID characteristics.

The high-latitude energy input strongly depends on the vertical component of the interplanetary magnetic field (IMF) B_z. The magnitude of the solar wind energy input can be approximated by solar wind–magnetosphere coupling functions. Newell et al. (2007) statistically analysed a set of 20 coupling functions and discussed their applicability for forecasting numerous geomagnetic activity indices. Since these coupling functions clearly correlate with AE and kp indices, it can be expected, that they also correlate with LSTID occurrences and thus may be suitable for their prediction. This hypothesis will be analysed, in this paper.

The work presented here uses an extended approach for description of TID occurrence, which neglects the phase information of the waves for the purpose of better indication of the wave presence and amplitude. This improves the preconditions for statistical analyses and generation of prediction models. We define the resulting parameter as a new TID activity index A_{TID}. In this work, we are demonstrating the capabilities of this TID activity index in characterising the occurrence of LSTIDs, show its correlation with solar and geomagnetic parameters potentially related to driving mechanisms and demonstrate an initial example how this index can be applied for generating a forecast model.

2. Data and methods

2.1. TID activity index

Radiowaves passing through the ionosphere are delayed, reflected, absorbed or scattered dependent on their frequency, because the ionosphere is a dispersive medium. Since the operating GNSS systems work with at least two different carrier frequencies, this allows the derivation of the Total Electron Content (TEC) along the line of sight between satellite and receiver. The derivation algorithms for TEC from GNSS observations are well described in e.g. Hofmann-Wellenhof et al. (2012).

The geometry free TEC is a precise estimation of relative changes along the line of sight TEC ($sTEC$) based on the difference between the two carrier phase signals. Commonly for the analysis of the TID signatures, a perturbation TEC (TEC_p) estimate is used, which is basically a high-pass filtered or band-pass version of the geometry free TEC signal. The TEC_p is derived for each satellite-receiver link (one observation of TEC between one ground station and one satellite from its rise to its decline) separately, by computing the difference between the original TEC signal (TEC) and a low pass filtered TEC or trend (TEC_{LF}).

$$TEC_p(t) = TEC(t) - TEC_{LF}(t) \tag{1}$$

Sometimes TEC_p is calculated from the $sTEC$ directly (Hernández-Pajares et al., 2006), and sometimes $sTEC$ is translated first into a vertical column TEC ($vTEC$) by applying a mapping function to the calibrated $sTEC$ (adjusting the integer ambiguity in the phase measurements, see e.g. Ding et al., 2007; Borries et al., 2009; van de Kamp et al., 2014), which is the method used in this work. For low-pass filtering (TEC_{LF}) either moving average (e.g. Saito et al., 1998; Shiokawa et al., 2002; Zakharenkova et al., 2016), polynomial fits (e.g. Ding et al., 2007; Habarulema et al., 2015) or other estimations of background TEC or trends (Hernández-Pajares et al., 2006) have been applied so far. There is no significant difference between these methods. Since so far, TEC_{LF} with about 60 min scale have been applied very successful for analysing LSTIDs, we will use it here, too. In some cases, not only low frequencies and trends are removed, but also frequencies higher than a certain threshold (Afraimovich et al., 2008). That means replacing $TEC(t)$ in Eq. (1) by another low-pass filtered TEC. Also in this study, we are using this kind of band-pass filter. We are extracting the variability in the temporal range of 30 to 60 min by calculating the difference between a moving average with 60 min window size and a moving average with 30 min window size.

$$TEC_{bp}(t) = \frac{1}{T_{30}} \sum_{n=t-0.5T_{30}}^{t+0.5T_{30}} vTEC(n) - \frac{1}{T_{60}} \sum_{m=t-0.5T_{60}}^{t+0.5T_{60}} vTEC(m) \tag{2}$$

T_{30} and T_{60} are chosen such that we get a 30 min and 60 min moving average, respectively, i.e, $T_{30} = 30/\Delta t$ and $T_{60} = 60/\Delta t$ where Δt corresponds to the sample time, which is equal to 30 s in this work. Fig. 1 shows in the left panel an example of geometry free TEC for the GNSS reference station GLSV on 17th March 2015. The middle panel shows the corresponding TID amplitudes for each satellite-receiver link (in different colours). We only use data with elevation larger than 60°. This derivation of TID amplitudes is identical to the derivation in Borries et al. (2009).

The new TID activity index is calculated again along each satellite-receiver link. For each time step t, the difference between the maximum TEC_bp and minimum TEC_bp in a window of 60 min size centred around this time step is calculated.

$$A_{TID}(t) = 0.5(max(\mathrm{TEC_{bp}}(x) * F(x-t)) - min(\mathrm{TEC_{bp}}(x) * F(x-t))) \tag{3}$$

For the window function F, we apply a Gaussian to reduce the impact of values with larger distance from the window centre. The resulting TID activity index A_{TID} is illustrated for the example in Fig. 1 in the right panel for each satellite receiver link in colours. These values have the georeference of the ionosphere pierce point and can be mapped to study the regional occurrence of TIDs. Next to generating maps of the TID activity index, also a TID activity index for one ground station can be calculated. In this case, a weighted mean of all A_{TID} estimates of this station measured at the same time is calculated. The weights depend on the elevation of the observation, to give highest weight to 90° elevation and reduce the weight with reducing elevation. Again a Gaussian function is used to set the weights.

Fig. 2 shows a map of the European–African sector with the GNSS ground stations, for which the TID activity index is calculated in this study. According to the authors knowledge, there does not exist yet a TID parameterisation like the TID activity index introduced here. The common TID indicators are comparable to TEC_p (Eq. (1)), which are very useful for extracting the respective wave parameters like wavelength, phase speed, period, azimuthal direction, etc. The TID activity index presented here just reflects the absolute amplitude of all waves

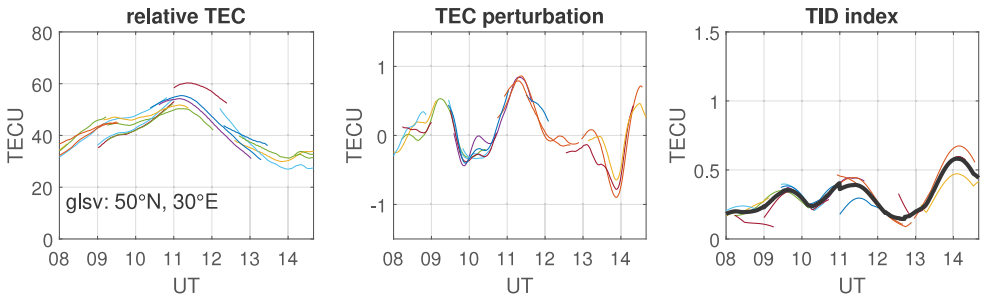

Fig. 1. GNSS derived TEC for the GNSS ground station GLSV on 17 March 2015. Left: geometry free TEC for all visible GNSS satellites (each satellite-receiver-link has a different colour). Middle: TEC_{bp} along each satellite-receiver-link, illustrating the TID amplitude. Right: TID activity index for each satellite-receiver link in colours and the weighted mean in black.

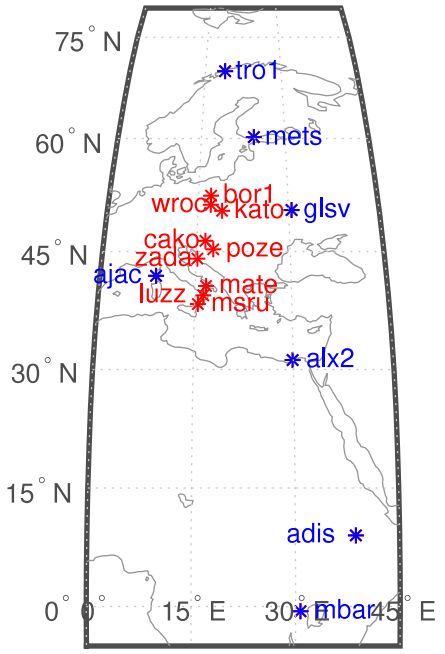

Fig. 2. Map showing the locations and ID of the GNSS stations used for the correlation analysis and the stations indicated in blue correspond to the stations used to generate Fig. 3.

present at a specific time. All other wave parameters are removed. It needs to be considered that the actual amplitude of all individual wave components can be estimated with classical spectral decomposition methods like Fourier transform only if it is a continuous signal. In nature, the amplitude of the waves typically varies with different conditions in the ionosphere–thermosphere system and often there are only individual non-continuous waves occurring (e.g. 24 Aug. 2005 presented in Borries et al., 2009). Spectral decomposition methods for transient signals like short-time Fourier transform or wavelet transform are better capable to capture the wave amplitudes, but often the wave power is distributed on different frequency components, either because the actual signal is a composition of multiple waves or because of mathematical effects like the leakage effect. The TID activity index presented is very simple to derive and does not suffer these problems.

2.2. Solar parameters and geomagnetic indices

For the purpose of forecasting TIDs, it is necessary to know, which geophysical parameters or indices do reflect their driving mechanisms. For the identification of these parameters and indices, we will apply cross correlation studies of the TID activity index with a list of potential candidates. The list compilation of the list of potential candidate parameters is described here.

Former studies showed relations of LSTIDs with the magnitude of geomagnetic indices kp, ap, Dst, AE and FAC (c.f. introduction). These will form the initial list of candidate parameters. The AE index has some limitations in the representation of the actual electrojet activity and Joule heating (Newell and Gjerloev, 2011). Thus, we add the SuperMAG Electrojet Indices SME and SML to our list. Considering that we are focusing the European region and local electrojet activity might matter, the list will be complemented by the IMAGE magnetometer electrojet index, which reflects best auroral electrojet activity in the European region. Also, the Polar Cap index for the northern hemisphere PCN is added to the candidates list, because it aims at monitoring the energy input from solar wind to the magnetosphere (loading activity). Kp, ap, Dst, AE, IE and PCN are available via different world data centres and websites (c.f. acknowledgement). Next to the common AE index, we also use the upper and lower AE indices AU and AL, which are reflecting the intensity of the eastward and westward auroral electrojet, respectively (Davis and Sugiura, 1966). Only FAC do not have an indicative index. A clear relationship between FAC and the polar cap potential has been shown in Adhikari et al. (2018). Also, FAC have been shown to be linearly dependent on different solar wind parameters, as shown e.g. in Iijima and Potemra (1982) and Korth et al. (2010), who performed a statistical assessment on this relationship. Therefore, we consider FAC to be sufficiently covered by the PCN and the merging electric field derived from solar wind parameters (to be discussed next). The auroral electrojet indices, $SYM-H$ and PCN are used with a 1 min temporal resolution. Kp, ap and Dst are used with their common temporal resolution of 3 h and 1 h respectively.

For the solar parameters, we start our list with the common IMF B_z component, because it is the most relevant parameter for the solar wind–magnetosphere coupling. In addition, we use the top five geoeffective parameters listed in the Newell et al. (2007) study, who performed a broad assessment on solar wind coupling functions and their relation to different geomagnetic indices and parameters. The top five coupling functions are:

- The Newell empirical parameter $d\Phi_{MP}/dt = v^{4/3} B_T^{2/3} \sin^{8/3}(\theta_c/2)$,
- The "intermediate" function $E_{WAV} = vB_T \sin^4(\theta_c/2)$,
- The Vasyliunas electric field $E_{WV} = v^{4/3} B_T \sin^4(\theta_c/2) p^{1/6}$,
- A modified version of the Akasufo ϵ parameter $\epsilon_3 = vB \sin^4(\theta_c/2)$,
- The Kan-Lee electric field $E_{KL} = vB_T \sin^2(\theta_c/2)$,

where v is the solar wind speed, B is the absolute IMF, $B_T = (B_y^2 + B_z^2)^{1/2}$ is the transverse IMF component, p is the solar wind dynamic pressure and $\theta_c = \arctan(B_y/B_z)$ is the IMF clock angle.

3. Results

3.1. Capabilities of the new TID activity index

A large number of GNSS station data is provided by the International GNSS Service (IGS), UNAVCO, EUREF and other networks. A

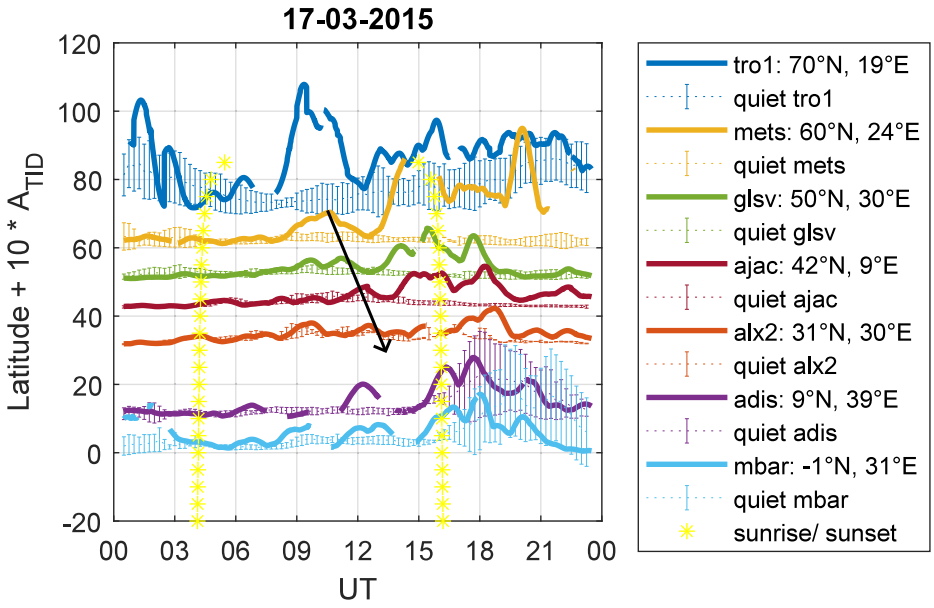

Fig. 3. TID activity index for 7 GNSS stations (as listed in the legend) during 17 March 2015. The TID activity index for each station is multiplied by 10 and the latitude integer has been added to illustrate the TID activity depending on latitude and time. A mean TID activity value and its standard deviation of the preceding 26 days is illustrated with error bars for each station. The two yellow almost vertical lines of asterisks indicate the sunrise and sunset times. The black arrow indicates the propagation of the LSTIDs activity from North to South.

subset of 7 stations, which are located in Europe and Africa in the longitude sector ranging 9–39°E at different latitudes, is used for the purpose of demonstrating the capabilities of the new TID activity index here. The IGS Identifiers and location of the stations are shown Fig. 2 (stations marked in blue). The illustration of the TID index for the St. Patrick's Day storm 2015 is shown in Fig. 3. For this event, the TID activity has been extensively discussed in several studies already (e.g. Zakharenkova et al., 2016; Borries et al., 2017; Liu et al., 2019a). To illustrate the TID activity index depending on latitude, we multiplied the TID activity index magnitude by 10 and added the latitude value of the station. The actual temporal evolution of the TID activity index for each station for the 17 March 2015 is presented with coloured bold lines. To distinguish significant amplitudes from normal quiet time activity, the mean and standard deviation of the preceding 26 days is presented for each station with thin dashed lines and error bars. Since the TID activity might depend on day–night conditions, we are indicating sunrise and sunset with yellow asterisks. In the example shown here, the TID activity is strongest in high latitudes (TRO1 station). The quiet time TID activity is larger in high latitudes than in mid-latitudes. In mid-latitudes, the quiet-time TID activity is lowest. During the storm event, the TID amplitudes exceed the quiet time level at all latitudes and they are significantly larger than the quiet time amplitude. The storm time LSTIDs start around noon. The largest amplitudes can be observed during sunset hours and in post-sunset conditions. Looking at the initial TID activity maxima at around noon in mid-latitudes, a delay is visible from North to South (indicated by the black arrow). This is related to the time which the LSTIDs need to propagate from the auroral region towards the equator.

At low-latitudes, a clear increase of the TID activity index is visible for quiet times in the post-sunset hours. This is the typical time for the occurrence of Equatorial Plasma Bubbles (EPB). At the low-latitudes stations, the storm-time TIDs exceed the quiet-time level during day, but not during night.

Fig. 4 presents the TID activity index observed in the European sector at mid-latitudes before (left panels) and during (right panels) the March 17, 2015 geomagnetic storm. The upper panels correspond to the TID activity index computed at the ionospheric piercing points and the lower panels corresponds to the TID activity index computed for the station location. A clear increase in the magnitude of the A_{TID} index during storm conditions can be observed, indicating LSTID activity.

3.2. Correlation of the TID activity with geomagnetic indices

For the correlation study, we are using a list of 60 geomagnetic storm events, characterised by significant ring current changes, which are indicated by a drop of the *Dst* index. The list of 36 event applied in the statistical study in Borries et al. (2009) is used as a starting point and is complemented by a list of more recent events. This complementary list is shown in Table 1. Both tables sum up to the 60 events used here.

Fig. 5 shows in a scatter plot the maximum TID index of the GNSS ground station GLSV (50°N, 30°E) during each event versus the maximum or minimum geomagnetic index in the 18 h preceding the time of the maximum TID index (marked as blue dots). In addition, we show with grey dots the relation between the maximum or minimum temporal derivative of the geomagnetic index and the maximum TID index. We add this analysis, to take into account the hypothesis that very sudden, strong changes in the auroral region thermosphere are generating the LSTIDs. It is well visible, how the TID activity increases with increasing magnitude of all the selected geomagnetic indices. We are adding regression lines in order to show the correlation of the parameters in the scatter plots. In most cases, there are outliers in the data sets, impacting the computation of the correlation. We are identifying these outliers using the Hampel filter method, which is detecting values that are more than three local scaled median absolute deviations from the local median in a moving window. They are marked with crosses in the scatter plots and excluded in the computation of the regression lines and the Pearson correlation coefficients. The corresponding Pearson correlation coefficients are indicated in each panel. This results in significant correlation coefficients for almost all parameters. The solid lines represent the regression lines. Even though a very large time period has been chosen for the statistical analyses, there is still only a limited number of severe storm events. All correlation values are larger than 0.5 indicating good correlation of the parameters. Only the derivatives of *kp* is not correlated. In most cases, the correlation of the maximum TID index with the derivative indices (grey dots) is larger than with the actual magnitude of the indices (blue dots). But, in most cases, this is not a significant difference. The correlation of the derivative of *ap* with the maximum TID index reaches 0.8 and is the best correlation coefficient obtained for the geomagnetic indices.

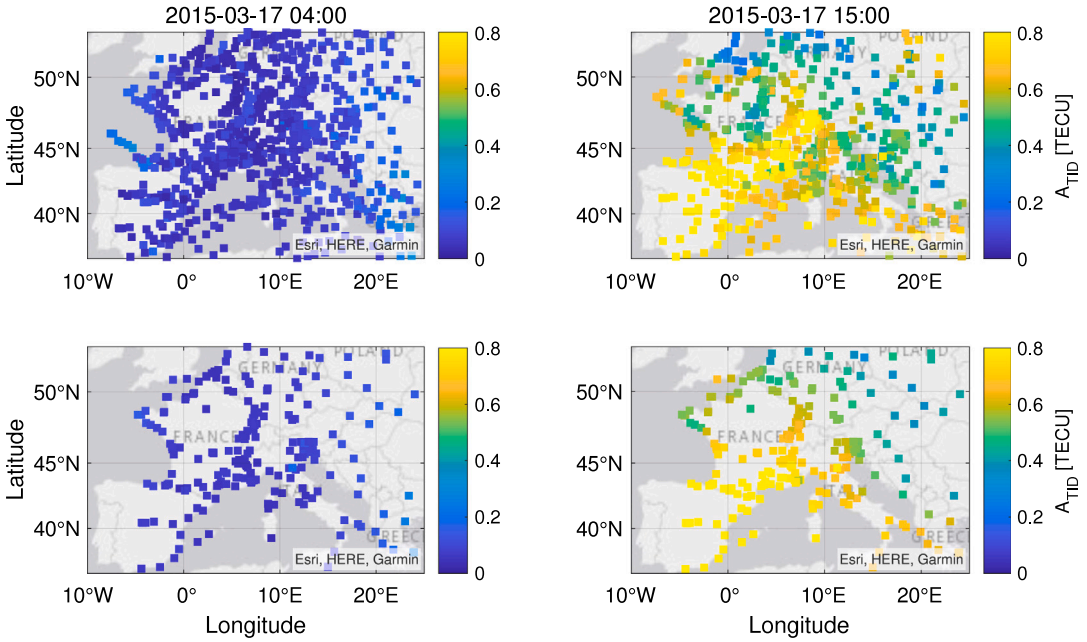

Fig. 4. TID activity index before (left panels) and during (right panels) the 17 March 2015 geomagnetic storm. The upper panels correspond to the TID activity index computed at the ionospheric piercing points and the lower panels corresponds to the TID activity index computed for the station location.

3.3. Correlation of TID activity with solar wind–magnetosphere coupling functions

Fig. 6 presents the correlation of the maximum TID activity index derived from the mid-latitude GNSS ground station GLSV with the maximum magnitude of the solar wind–magnetosphere coupling functions in the same way like it has been done for the geomagnetic indices. Similar to the geomagnetic indices, the TID activity increases with increasing magnitude of all the selected parameters. In this case, the correlation of the derivative parameters in general is smaller than the correlation with the absolute magnitude of the parameters. However, the difference is not significant. The normalised correlation coefficient for the absolute magnitudes of the parameters ranges between 0.76 and 0.80. The highest correlation coefficients result from $\epsilon 3$ and E_{KL}. The correlation coefficients of all solar wind based geoeffective parameters are very similar. In fact, the magnitude of the correlation is larger than for most of the geomagnetic indices.

3.4. Latitudinal dependence of correlation

Because the TID activity changes significantly with latitude, as demonstrated in Fig. 3, our next step is to assess how this impacts the correlation values of the TID activity index with the geophysical parameters. The same analysis presented in Figs. 5 and 6 for the GLSV station is now applied to a number of stations in the European–African sector. The location and ID of these stations is shown in Fig. 2 (red and blue stations). In order to keep a good overview in this analysis, we limit the amount of geomagnetic and solar parameters. We select only those, which showed best correlation for the GLSV station. And in case where indices are very closely related like for $SYM-H$ and Dst and AE and AL, we only use the most common one.

In Fig. 7, the correlation coefficients between a geomagnetic or solar-wind parameter and the TID index for each individual GNSS station is plotted versus the latitude of the respective station. The correlation coefficients with the absolute magnitude of the parameters are shown in filled black and grey dots, while the correlation coefficients with the derivatives of the parameters are shown in blue circles. The dots and circles are not labelled with the station ID, because this is considered irrelevant for the discussion of the results. Instead, the dot's and circle's size and colour intensity are indicating how many out the total 60 events were included in the statistics (not each station is delivering data for each event). If the shown correlation coefficient is based on all 60 events (100%), the dot is largest and has strong black or blue colour. The smaller the fraction of available data sets, the smaller the corresponding dot or circle and the lighter its colour.

It can be seen that for all stations, the correlation coefficients of the absolute magnitude and the derivative magnitude with the TID index are rather close to each other. In most cases, the correlation coefficient with the derivative is smaller, but there are also a few cases where the correlation with the derivative parameter is larger. The deviations between the correlation coefficients of the absolute and the derivative parameters are usually larger for smaller data availability. This is related to the larger uncertainty for smaller data availability.

It is also well visible that the correlation coefficients for all parameters are largest in the latitude range 30–50°N. In high and low latitudes, the correlation coefficients hardly exceed the magnitude of 0.5. There is not much difference between the different solar and geomagnetic parameters. On average, the highest correlation coefficients are reached for E_{KL}, reaching values up to approximately 0.8, which suggests that it may be a good indicator for LSTIDs occurrence and a promising parameter to be used on the prediction of LSTIDs activities at mid-latitudes in the European region.

4. LSTID forecasting, a demonstration

In this section, we investigate and demonstrate the applicability of the proposed index on the LSTID activity forecasting. From the results presented in Fig. 6, one can note that there is a good correlation between the maximum TID activity index and the maximum Kan-Lee electric field E_{KL} observed within the 18 h prior to the maximum TID activity index. Our objective in this section is to derive coarse-grained predictions of the maximum A_{TID}, based on a linear regression approach. This task is performed as follows: since the correlation investigation presented in Figs. 5 and 6 has been conducted by analysing

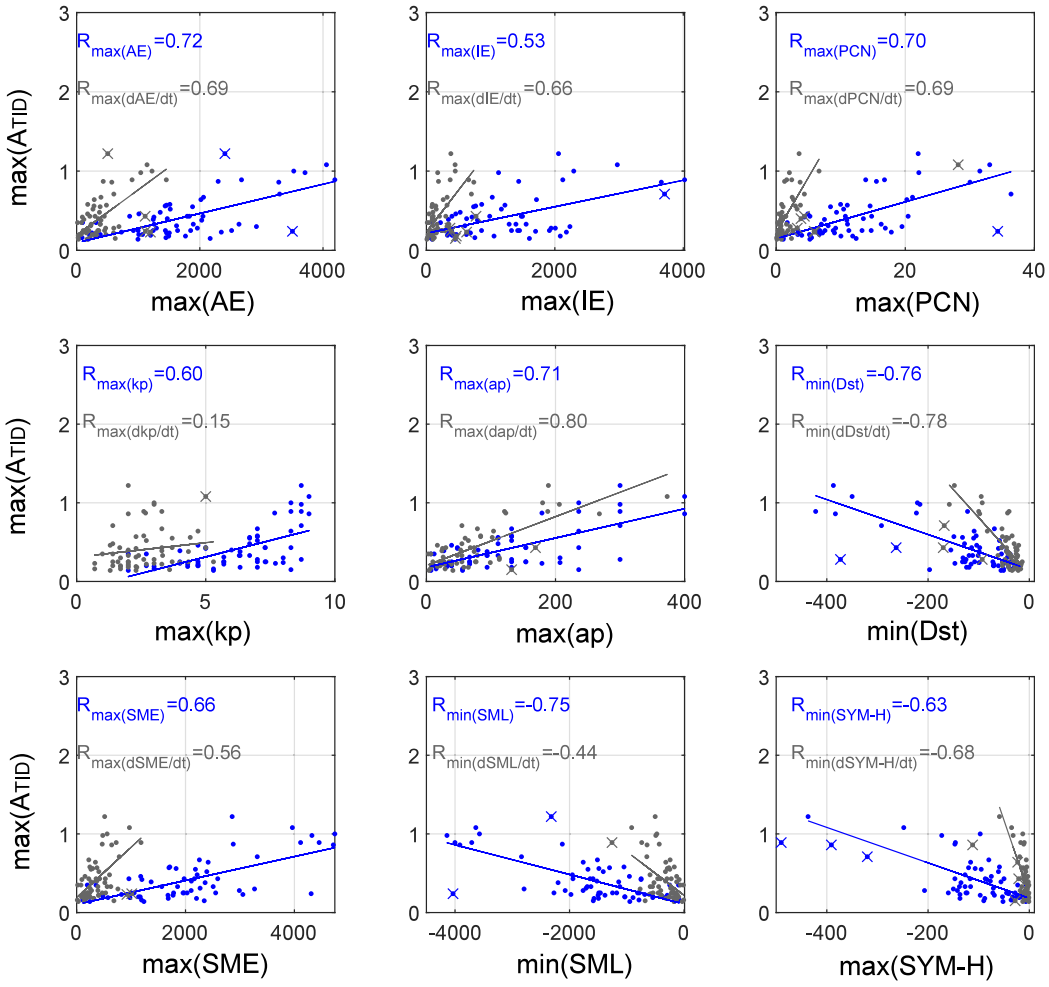

Fig. 5. Scatter plots of the maximum TID activity index (y-axis) of the GNSS ground station GLSV during each of the 60 storm events versus the maximum geophysical parameter (x-axis) in the 18 h ahead of the maximum TID activity index (minimum for Dst and $SYM-H$). Top left: AE index, top centre: IE index, top right: PCN, middle left: kp index, middle centre: ap index, middle right: Dst index, bottom left: SME index, bottom centre: SML index, bottom right: $SYM-H$ index. Grey dots indicate the temporal derivative indices respectively. The text in each panel describes the Pearson correlation coefficient derived from the respective indices. The solid lines are the regression lines derived for the actual index (blue) and its derivative respectively (grey). Outliers are indicated with crosses.

the maxima values, the maximum EKL in a 2 h interval ($max_{2hr}E_{KL}$) is computed. Different intervals could be used, but we have empirically chosen 2 h, aiming at maximising the prediction performance. The obtained values $max_{2hr}E_{KL}$ are then applied to a linear regression equation to predict the A_{TID}.

In order to derive the linear regression equation, we use an approach based on the leave-one-out cross-validation, in which one event from the n geomagnetic storm events presented in Fig. 6 is used for validation, and the other $n-1$ events are used to derive a linear regression model that will be used for the A_{TID} prediction on the validation event. We are generating n linear regression models, each with another storm event kept for validation. This allows to use all the available geomagnetic storms for the validation of the proposed approach. Fig. 8 illustrates the linear regression fit $y = b + ax$ (with $b = 0.152 \pm 0.036$ and $a = 0.021 \pm 0.002$, significant with a p-value of 2.6e-12.) and the 95%, 90% and 50% prediction intervals used for predicting the A_{TID} for the geomagnetic storm event observed on the 20 of November 2003. This was a strong storm that occurred due to an Interplanetary Coronal Mass Ejection (Zhang et al., 2007) that reached the Earth in the morning of the 20 of November 2003 and led to a Dst index of approximately −422 nT at 21 UT (Blanch et al., 2005). The TID analysis for this particular storm is presented in Borries et al. (2017).

For this geomagnetic storm, for example, we have used the following simple linear equation, which is based on the linear regression fit presented in Fig. 8:

$$\hat{A}_{TID}(t+n) = 0.152 + 0.021 \times max_{2hr}E_{KL}(t), \quad (4)$$

where $max_{2hr}E_{KL}(t)$ corresponds to the maximum EKL in a 2 h interval and n represents the 30, 60, ... 180 min predictions time, which are then compared to the A_{TID} reference values at t, $t+30$, ..., $t+180$.

Fig. 10 shows the result of the one-hour prediction for the period from 19 to 21 of November 2003. The A_{TID} computed for the GLSV station during this event reached magnitudes of around 0.8 TECU, indicating a moderate/strong TID activity over the station. For this period, one can note that the prediction model is able to reproduce the increase of the A_{TID} observed during the storm. Rapid fluctuations are, on the other hand, not very well reproduced. In this event, the predictions lead to a Root Mean Squared Error (RMSE) of 0.16 TECU and a Pearson correlation coefficient (R) of 0.84.

As presented in Fig. 10, although the proposed model is not able to reproduce the rapid fluctuations, it can depict fairly well the significant increases in the TID index during storm events. With this in mind, and taking into consideration that, in practice, any regression problem for a continuous variable can be simplified as a classification task by introducing thresholds and separating the range of classes (Camporeale, 2019), we evaluate the performance of the model on the LSTID activity detection over the GLSV station for all the aforementioned geomagnetic storm events.

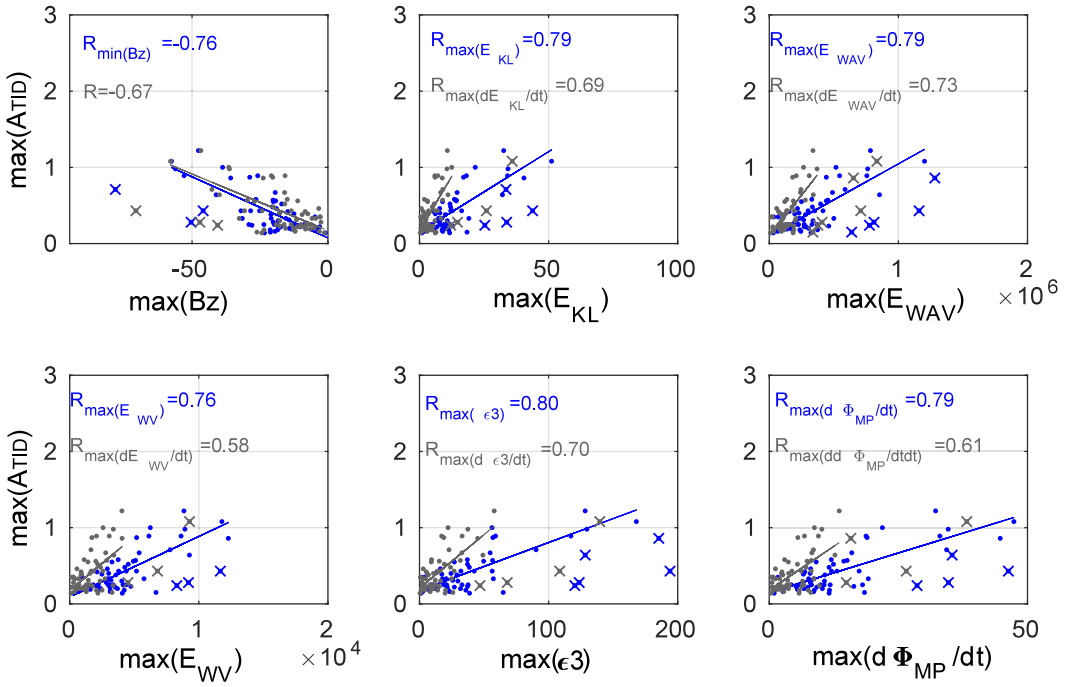

Fig. 6. Scatter plots of the maximum TID activity index (y-axis) of the GNSS ground station GLSV during each of the 60 storm events versus the maximum geophysical parameter (x-axis) in the 18 h ahead of the maximum TID activity index (minimum for IMF Bz). Top left: IMF Bz, top centre: Kan-Lee electric field E_{KL}, top right: "intermediate" function E_{WAV}, bottom left: Vasyliunas electric field E_{WV}, bottom centre: variant of the ϵ parameter, bottom right: Newell empirical parameter $d\Phi_{MP}/dt$. Grey dots indicate the temporal derivative parameters respectively. The text in each panel describes the Pearson correlation coefficient derived from the respective parameters. The solid lines are the regression lines derived for the actual parameter (blue) and its derivative respectively (grey). Outliers are indicated with crosses.

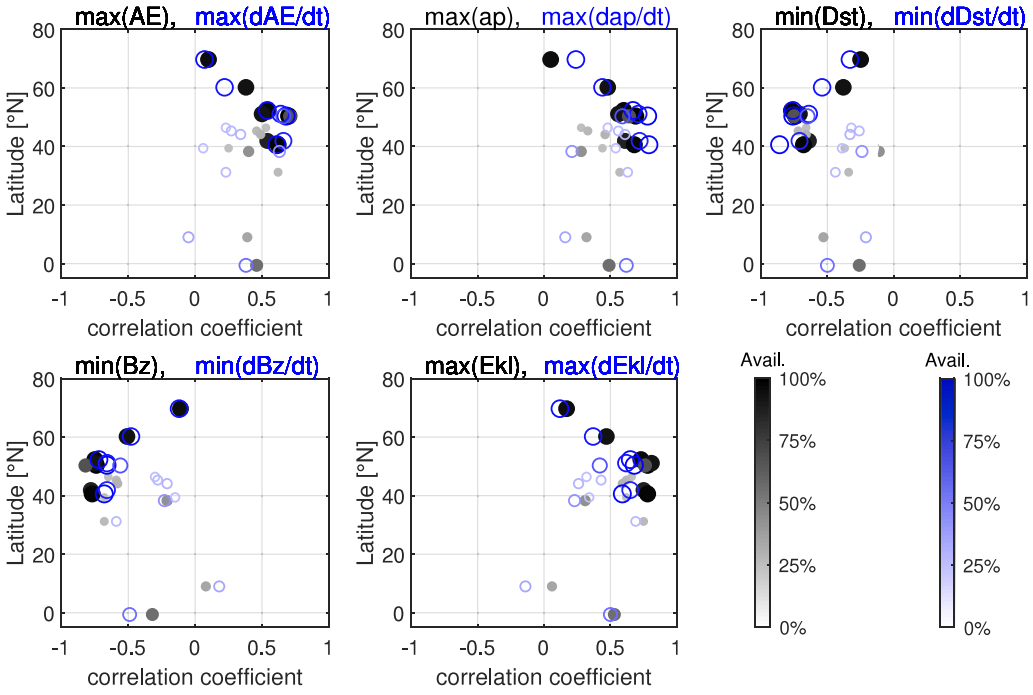

Fig. 7. Scatter plot of the correlation coefficient between the maximum TID index and the parameter given in the title of each panel. The intensity and size of the dots indicates the data availability for the correlation coefficient. The most intense colour (black or blue) is 100% data availability. The filled black/grey dots are for the absolute magnitude of the parameter. The blue circles are for the derivative of the parameter.

4.1. Prediction performance evaluation

We have set different thresholds based on the 90th, 97.5th and 98th percentiles of the A_{TID} considering all values and all events, corresponding to thresholds of 0.2, 0.3 and 0.5 TECU, approximately. According to this approach, every prediction point of A_{TID} greater than or equal to the threshold level is considered a LSTID activity event and prediction points below this threshold are considered as non-LSTID activity events. This type of classification leads to the following possibilities when comparing to the reference values: True Positive (TP), True Negative (TN), False Positive (FP) and False Negative (FN). Fig. 9 shows how this classification would work in a fictitious scenario

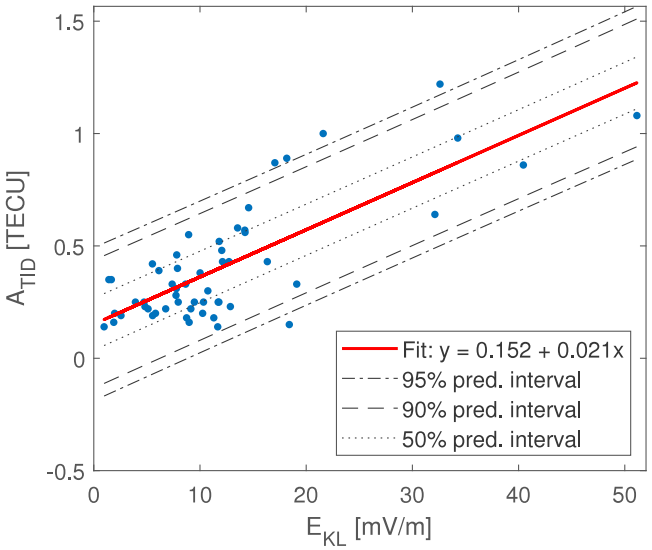

Fig. 8. Scatter plot of the maximum TID activity index of the GNSS ground station GLSV during each of the 56 storm events versus the maximum Kan-Lee electric field E_{KL} in the 18 h ahead of the maximum TID activity index. Outliers indicated in Fig. 6 are not included.

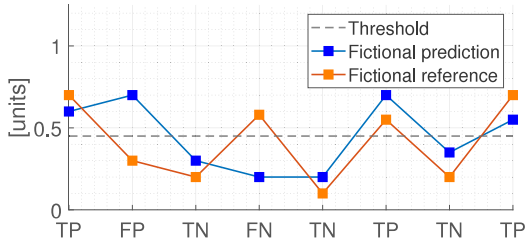

Fig. 9. Illustrative example of classification as TP (true positive), FP (false positive), TN (true negative), and FN (false negative) for a fictitious scenario with a threshold of 0.45 TECU.

comparing sequences of predicted and reference values. The class for each sample is indicated in the horizontal axis. In this example, one can observe 3 TP, 1 FP, 3 TN and 1 FN predictions.

In order to evaluate the performance of the model in predicting the occurrence or not of LSTID activity events, we have assessed the True Skill Score (TSS), which gives the difference between true and false positive rates and is unbiased with respect to class-imbalance (Detman and Joselyn, 1999; Camporeale, 2019). TSS ranges between −1 and 1, with −1 to be interpreted as always wrong predictions (Bobra and Couvidat, 2015), 0 or less indicating a performance no better than random (Detman and Joselyn, 1999) and 1 indicating perfect forecasts. The TSS is computed based on the following equation

$$\mathrm{TSS} = \mathrm{TPR} - \mathrm{FPR} = \frac{\mathrm{TP}}{\mathrm{TP}+\mathrm{FN}} - \frac{\mathrm{FP}}{\mathrm{FP}+\mathrm{TN}}, \tag{5}$$

which is based on the difference between true positive and false positive rates, indicated as TPR and FPR, respectively (Camporeale, 2019). For the illustrative example shown in Fig. 9 a TSS of 0.5 is observed.

In order to evaluate the prediction performance of the proposed model we used as a benchmark the persistence model, which assumes that a future value A_{TID} is equal to the most recent observation (Reikard, 2018). Fig. 11 shows the resulting TSS for the linear regression model (lines with squares) and the persistence model (lines with triangles) for the three selected thresholds. The tested prediction lead times range between 0 and 180 min. For the lead time of 0 min (nowcast), the persistence model reaches the maximum achievable TSS of 1 because it is identical to the ground truth. For lead times larger than 30 min and the thresholds of 0.3 and 0.5, the TSS of the linear regression model is larger than the TSS of the persistence model. The TSS for lead times larger than 30 min reaches maximum values between 30 and 60 min lead times and decreases continuously for larger lead times. The best performance is obtained by the linear regression model using a threshold of 0.5 TECU and a prediction time of 30 min, leading to a TSS of 0.802 (compared to a TSS of 0.608 of the persistence model with the same lead time and threshold). The TSS for the linear regression model with a threshold of 0.2 TECU is lowest with values of 0.35, not fluctuating much for different lead times.

5. Discussion

5.1. TID characteristics

LSTID and MSTIDs usually have different sources and are therefore studied separately. Since both signatures usually differ in their temporal and spatial scale, the adjustment of the right filter in the derivation of the TID index A_{TID} allows the separation of both effects. Based on the description of TID scales in Hunsucker (1982), LSTIDs have periodicities of 30–180 min, while MSTID periodicities range between 15 to 60 min. The wavelength of MSTIDs is in the range of tens to hundreds of km, while LSTIDs typically have 1000 km wavelength and beyond. The selection of a bandpass filter with a 10–30 min filter window should allow the separate study of MSTIDs. In the example study presented here, a high-pass filter with 60 min and a low-pass filter with 30 min was applied. We did not extend the filter size to 120 min on purpose because then the strong daily variability is impacting the results. It is expected that mainly LSTIDs should be included in the TID activity index analysed here. However, since there is an overlap in the temporal scales of the MSTIDs and LSTIDs in the applied filter range, both TID types cannot be separated completely. But, in mid-latitudes storm–induced LSTIDs commonly have larger amplitudes than MSTIDs (reflected by the difference between quiet- and storm-time A_{TID} curves shown in Fig. 3), and thus large amplitudes of A_{TID} should reflect LSTIDs only. For the purpose of clear separation of the different TID effects, a spatial filter for specific ranges of the wavelength should be applied to TEC_{bp} before the computation of A_{TID} and mapping. This requires a sufficiently dense data coverage of TEC_{bp} and includes the challenge of view-angle dependent MSTID signatures and correct mapping, as discussed e.g. in Nykiel et al. (2019). In the case of the station based TID index, which is a focal point of the results discussed here, the spatial filtering is not possible.

The quiet time TID activity index is a good indicator of the noise level and uncertainties of the TID activity index. In the present study, it may also contain regular MSTID occurrence, as discussed above. Also, the passage of the solar terminator, which can give rise to LSTIDs (Song et al., 2013), may generate a peak during the solar terminator passage in the morning. Low quiet time amplitudes are observed for the mid-latitude stations (METS, GLSV, AJAC and ALX2, c.f. Fig. 3). No terminator signatures are visible for these stations in this case study and were also not found in longer time series studies (not shown here). The equatorial and low-latitude stations (MBAR and ADIS) show large amplitudes and standard deviation of the quiet-time TID activity index after sunset. This is the typical time and location of EPBs and scintillation activity. They are associated with strong TEC perturbations at different temporal scales. It has already been shown decades ago that AGWs can seed EPBs (Tsunoda and White, 1981; Singh et al., 1997). Modelling results (Krall et al., 2011) and also observations from the GOLD mission suggested that AGWs with periods of up to 1 h can trigger EPBs (Eastes et al., 2019; Chou et al., 2020). Thus, the periodicity of storm–driven LSTIDs investigated in this work and the signatures of AGW seeding EPBs are very similar and can both create strong A_{TID}. Also, it cannot be excluded that the EPB itself creates a

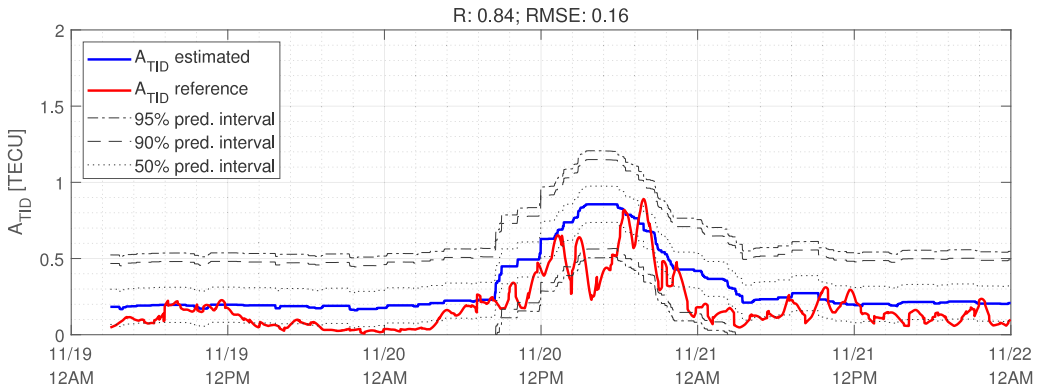

Fig. 10. Prediction of the TID index (blue line) and reference values (red line) for the geomagnetic storm observed on the 20th of November 2003. 95%, 90% and 50% are indicated with the black dashed lines.

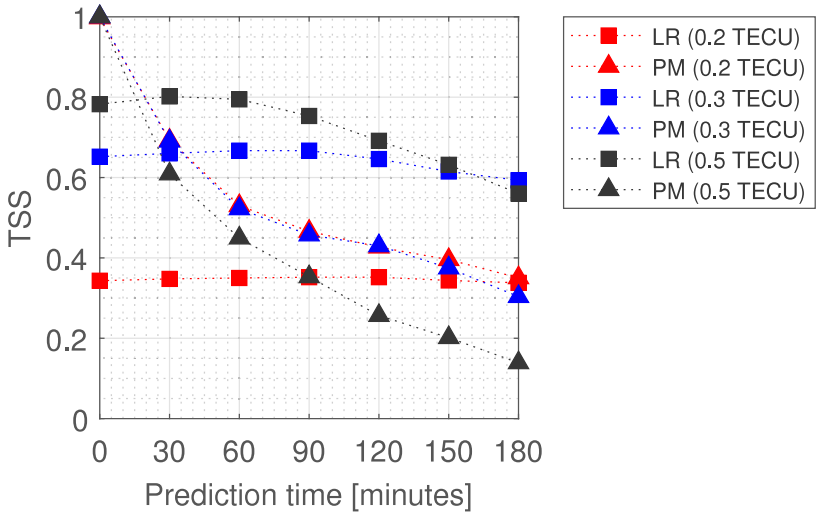

Fig. 11. True Skill Score for the predictions based on the linear regression (LR) and persistence model (PM) for different thresholds (in parenthesis) and different prediction times. The threshold determines the criterion to determine the occurrence or not of a LSTID activity event.

TID-like signature in the TEC observation. Because of the regular occurrence of enhanced A_{TID} at low latitudes in the evening hours, it can be assumed that it will contain mainly the signature of perturbations related to EPB, although contributions from storm–driven atmospheric gravity waves will be included occasionally, too. The distinction of the storm–driven LSTIDs from EPB related effects needs a more detailed analysis. Either characterisation of the EPB related signatures or a better applicable filtering is suggested. This goes beyond the objectives of the present work. Also, the high-latitude station (TRO1) shows larger quiet-time TID activity amplitudes. Auroral activity, precipitation and patches can be the source of these fluctuations, which often have much larger magnitudes than LSTIDs in mid-latitudes. Tromsø is typically within the auroral oval, and during storm conditions, it may even be within the polar cap. Since storm–driven LSTIDs are typically generated at the equatorward edge of the auroral oval (Borries et al., 2017), the TID activity index at Tromsø is most likely not related to them. There exist numerous studies reporting MSTIDs in the polar region, including correlations to AE index (e.g. Vlasov et al., 2011; Negale et al., 2018). In a case study of September 2017, Zhang et al. (2019) showed that these storm–induced nightside TIDs from the polar cap to auroral zones are equatorward, while dayside TIDs (around midday) of these regions are propagating poleward. Thus, TIDs in the polar and auroral regions have very different characteristics and need to be treated differently. Also, it will be necessary to analyse if polar patches (which have significant amplitudes) impact the magnitude of the TEC_bp, before assessing any wave characteristics in this region.

In the case study shown in Fig. 3, which is for storm conditions on 17 March 2015, the TID activity index increased well above the quiet time level at all stations. It started with a perturbation between 9 and 12 UT and then continued after 14 UT. This is consistent with the discussion of LSTIDs during this event in Borries et al. (2016), Zakharenkova et al. (2016), Liu et al. (2019a) and Lu et al. (2020). Also, the equatorward propagation of the LSTIDs can be tracked with the TID activity index (e.g. the peak starting at about 14 UT at METS and arriving at about 17 UT at MBAR).

5.2. Correlation with geophysical parameters

We are investigating the correlation of the TID magnitude with the magnitude of geophysical parameters, because the correlation may provide hints for the generation mechanisms. However, the generation of TIDs is a complex process which is not yet completely understood. A few thermosphere and ionosphere conditions may impact their generation. Thus, the magnitude of the TIDs may not clearly correlate with the solar wind energy input represented by the geoeffective parameters. Outliers may indicate different background conditions for the TID

generation. In our correlation studies, outliers have been removed in order to generate better conditions for modelling and prediction. Thus, our results represent the average response to geophysical conditions. However, the outliers are specifically interesting from the physical point of view. They impose the question of why no significant LSTIDs are generated in the European–African sector despite significant energy input from the solar wind and related significant geomagnetic disturbances. We do not yet have a sufficient amount of outliers for statistical analysis. Thus, they need to be analysed in a qualitative way. Four strong events with missing significant LSTIDs have been detected in our analysis: 21-Jan-2005, 07-Nov-2004, 15-May-2005, and 06-Nov-2001. There are also outliers in the opposite sense. Strong LSTIDs have been measured when there was only moderate solar wind energy input, like 24-Nov-2001. Both cases, the lack of strong LSTIDs and unexpectedly large LSTIDs, are ideal subjects to study more in depth the generation mechanisms of LSTIDs. This is beyond the scope of this work and needs to be done in a follow–up study.

The correlation of LSTID occurrence with different geomagnetic indices, presented in earlier studies by different authors, is supported by the correlation results presented here. In fact, all geomagnetic indices are correlated with the LSTID magnitude. IE, kp and $SYM-H$ have the lowest correlation, while AE, SML and Dst show the best correlations. The high correlation of AE and TID of 0.8 in Borries et al. (2009) had been achieved by distinguishing day and night and solar max and solar min conditions. Because this classification has not been applied here, the correlation values presented here are slightly lower. The correlation of SML, representing the westward electrojet, is larger than that of SME and AE. Also, the comparison of the correlation coefficients of AU and AL indices (not shown here) indicate that mostly the westward electrojet (represented by AL) is relevant for the TID magnitude. Since Singh et al. (2015) discuss that during extreme geomagnetic activities, AL index could represent substorms better than AE index, SML and AL might be preferred against SME and AE for the purpose of LSTID prediction. But, in our analysis, we do not see a significant difference between both. Since we are presenting an analysis of stations in the European–African sector, it can be assumed that the IE index may correlate best, because it is based on a European magnetometer chain. But, our results show that this is not the case. Thus, it is considered that global energy deposition is more relevant for the LSTID generation than local effects.

The correlation of LSTIDs with solar wind parameters has not been shown before. It reaches the same magnitude as the correlation with geomagnetic indices and even exceeds it slightly. There is no significant difference in the correlation results for all the different solar wind–magnetosphere coupling functions applied here. The correlation coefficients of the TID magnitude with the solar wind parameters reach almost 0.8, indicating a very good correlation. In fact, this magnitude is comparable with the correlation results presented in Newell et al. (2007). There, the maximum correlation coefficient was 0.85. This magnitude indicates good potential for prediction. Thus, based on the presented results, we suggest common solar wind parameters like E_{KL}, $\epsilon 3$, and IMF B_z component to be used for the prediction of LSTIDs.

We add the temporal derivatives to the correlation analysis in order to take into account the hypothesis that very sudden, strong changes in the auroral region thermosphere are generating the LSTIDs. In the case of the solar wind parameters, the temporal derivatives generally show lower correlation values. In the case of the geomagnetic indices, the correlation values improved by using the temporal derivative in some cases. However, it did not exceed the correlation values of the solar wind parameters. Thus, sudden changes in the magnetosphere–ionosphere–thermosphere system are relevant for generating LSTIDs, but they cannot be traced back to sudden changes in solar wind conditions.

The analysis of A_{TID} at stations with different latitudes in the European–African sector showed that only mid-latitude stations show good correlation with solar and geomagnetic parameters. In high latitudes, the correlation values drop significantly and tend to zero at Tromsø (TRO1). That the large magnitudes of A_{TID} at Tromsø are not related to LSTIDs has been discussed in Section 5.1 already. This explains well the low correlation results at these latitudes. During strong storms, the auroral oval extends significantly. Thus, a station at 60°N will often be in the auroral region during storms, and their correlation with LSTID magnitudes decrease. In the European–African sector, the auroral oval hardly reaches latitudes of 50°N. Thus, the correlation results reach maximum values there.

In low and equatorial latitudes, the number of available GNSS data sets for the selected storms is not so high and therefore, the correlation results are not as reliable as those obtained in mid-latitudes. The correlation values at the geomagnetic equator, which is at about 10°N in the African sector, tend to be zero. In the crest region, at the geographic equator, the correlation value reaches a moderate value of 0.5. A decrease in the correlation results is expected in this low-latitude and equatorial region because A_{TID} includes the signature of AGW causing EPB (c.f. Section 5.1).

Concerning the confidence of the presented correlation results, we consider two facts supporting the validity of the shown results: First, the good agreement of the correlation values between the different solar and geomagnetic parameters and second, the good agreement of the correlation coefficients of the absolute magnitude of the parameters and their derivatives (Fig. 7).

It can be argued that the correlation of the TID activity index with geomagnetic and solar indices is not linear as assumed for the regression analysis presented here. Therefore, we had a detailed look into the different results and also tested nonlinear dependencies between maximum A_{TID} and maximum geomagnetic and solar indices. We performed calculations for the GLSV station (the results are listed in Table 2). The most significant change was noted for the kp index. After raising to the second power or using the square root of the exponential value, we obtain correlation coefficients higher by 0.05 and 0.10, respectively, reaching a correlation value of 0.70 (with a p-value of 5.0e-10). Still, this improved correlation value for nonlinear kp functions does not exceed the linear correlation of many other geomagnetic indices, including ap. This shows that the logarithmic scale of kp is not ideal for describing and modelling the physical processes like LSTIDs. It has been discussed before the changes over time in the solar wind–based parameters have less correlation with maximum A_{TID} than the original parameter. The correlation of these temporal derivatives (of dE_{KL}/dt, dE_{WAV}/dt, and $d\epsilon 3/dt$) can be improved using the square (we noted an increase in correlation of 0.04, 0.02, and 0.05, respectively). Still, they do not reach the magnitude of the original parameter's correlation (E_{KL}, E_{WAV}, and $\epsilon 3$) and are thus not recommended for use in the modelling and prediction of LSTIDs. No remarkable improvement with nonlinear relationships was found for the other indices.

5.3. TID prediction

In Section 4, the predictability of LSTIDs has been demonstrated in an easily understandable approach using linear regression. It allows us to explain some peculiarities which need to be considered for prediction. First, it is necessary to take into account that the TID activity index shows some fluctuations, which are not related to solar wind conditions or geomagnetic indices perturbations. These are visible in Fig. 10 comparing the red and blue lines. Since it is not completely understood how these fluctuations develop (changing thermospheric conditions can be a cause), the LSTID prediction model aims to predict the maximum achievable TID index A_{TID}. The resulting prediction (Fig. 10, blue line) is like an upper envelope function of the observed A_{TID} (Fig. 10, red line). Hence, typical model evaluation methods like RMSE and correlation coefficients are not ideal for evaluating

the model's performance. Computing skill scores based on the contingency table is better suited for this purpose. This validation method has already been successfully applied many times for space weather modelling and prediction (e.g. Bloomfield et al., 2012; Welling et al., 2018; Verkhoglyadova et al., 2020; Mukhopadhyay et al., 2020; Kahler and Darsey, 2021). The TSS is a common skill score relevant for data sets with class-imbalance, as is the case with the occurrence of LSTIDs. The class-imbalance here arises due to the fact that the majority of data samples do not contain increased LSTIDs activity. The application of the contingency table requires the definition for event detection. We tested the method using three different thresholds based on the statistical occurrence of A_{TID} magnitudes in the list of events studied here. As shown in our results, the TSS strongly depends on the proper threshold definition. The threshold of 0.2 TECU is obviously chosen as too low for the linear regression model. The reason is visible in Fig. 8. Here, the regression line starts at y = 0.152, and the 50% prediction interval reaches up to about 0.25. Thus, already in quiet times the model will fluctuate around a value of 0.2 TECU and the validation with the contingency table and a threshold of 0.2 TECU will result in many FP values. This shows that the presented LSTID prediction model is rather restrictive, showing most of the time, the chance of getting a LSTID with 0.2 TECU amplitude. That this restriction is not wrong shows a recent study by Thaganyana et al. (2022), who presented an analysis of TIDs with medium to large scales in the European–African sector travelling from one hemisphere into the other. They occurred during geomagnetically quiet days and were associated with tertiary AGWs generated from the dissipation of secondary AGWs excited by the local body force created from breaking mountain waves (according to the theory of, e.g. Becker and Vadas, 2020).

Better performance in the prediction of LSTIDs is shown for larger thresholds, i.e. stronger events. The best model performance is shown for a threshold of 0.5 TECU. This indicates that this model is best suited for the prediction of moderate/strong TID activity just by means of solar wind data. In addition, the model performance is best for lead times between 30 and 60 min. Assuming that the LSTIDs are excited at the equatorward boundary of the auroral oval (Borries et al., 2017), which is on average at about 65–70°N in the European region, and a speed of 680 ms^{-1} (Borries et al., 2009), the LSTID would need 40–54 min to reach the GNSS station GLSV at 50°N, which has been used for the demonstration of the prediction model. This matches well with the derived best lead times of the prediction model. This estimation also shows that the model assumes an immediate impact of the solar wind on the ionosphere, which is confirmed by the performance. The estimation of LSTID propagation time only applies to the beginning of the storm. Later in the course of the storm, when the auroral oval is larger, The LSTIDs need less time to reach the mid-latitude GNSS station.

The theory about the existence of AGW and TID in the thermosphere and ionosphere goes back many decades. Since then, models have been developed to theoretically describe the wave signatures (e.g. Hocke and Schlegel, 1996; Fedorenko et al., 2013, and references therein). These models depend on good and realistic parameterisation. A combination of such theoretical models with the prediction model described here may have the potential for even more realistic TID predictions in future.

6. Summary and conclusion

A new TID index A_{TID}, based on an easy extension of the commonly used approach for TID detection, neglecting the phase information of the waves for the purpose of better indication of the wave presence and amplitude, is introduced. A_{TID} has been developed to facilitate and foster statistical analyses of TIDs because of its good quantification of the temporal and local occurrence and strength of TIDs. This TID activity index can be applied for individual GNSS station (like demonstrated here) and also for mapping TID activity over larger regions or globally. It is not only capable of studing LSTIDs (as shown here), but it can also be applied for analyses of MSTIDs (10–30 min period). However, the present study also reveals that A_{TID} applied with a 30–60 min filter window does not allow to distinguish MSTIDs and LSTIDs.

The presented work demonstrates that A_{TID} is well applicable for statistical analyses. Correlation studies revealed that LSTID magnitudes are well correlated with solar wind parameters like the Kan-Lee merging electric field. Thus, the magnitude of the global solar-wind energy input into the Earth's magnetosphere–ionosphere–thermosphere system is most relevant for the LSTID generation. The good correlation indicates that common solar wind parameters and IMF B_z component can be used for the prediction of LSTIDs. The correlation with common geomagnetic activity indices showed that also sudden changes in the magnetosphere–ionosphere–thermosphere system are relevant. It needs to be considered that all correlation results are only good for mid-latitude stations. High-latitude regions are strongly impacted by auroral processes, and low-latitude regions by AGWs coupling from below. Based on the results presented here for low- and equatorial latitudes, we suggest investigating if A_{TID} can be used in conjunction with EPB analysis and prediction.

The usage of the introduced TID index A_{TID} allows the modelling and prediction of TIDs. The development of a prediction model for storm–induced LSTIDs based on solar wind observations only has been demonstrated. It shows very good performance in predicting LSTIDs in mid-latitudes. The model also indicates that there is a quiet time perturbation level of about 0.2 TECU in the mid-latitude region in Europe, most likely related to AGWs coupling from below.

Declaration of competing interest

The authors declare that they have no known competing financial interests or personal relationships that could have appeared to influence the work reported in this paper.

Data availability

Data will be made available on request.

Acknowledgements

The authors would like to thank the Brazilian agencies National Council for Scientific and Technological (CNPq) and the Federal District Research Support Foundation (FAPDF) that partially supported this work. GN acknowledges support from the Gdańsk University of Technology by the DEC-13/2022/IDUB/II.1/AMERICIUM grant under the AMERICIUM — "Excellence Initiative - Research University" program. For generation of the TID activity index, we used RINEX files from IGS for the dates before 2015 and processed line of sight TEC data from Madrigal database. For the geophysical parameters, we used ACE solar wind data from ACE-MAG, ACE-SWICS and ACE-SWEPAM instruments www.srl.caltech.edu/ACE/ASC/level2/, the auroral electrojet indices AE, AU, AL as well as the ring current index SYM-H from https://wdc.kugi.kyoto-u.ac.jp/aeasy/index.html, the Disturbance strom index Dst from https://wdc.kugi.kyoto-u.ac.jp/dstae/index.html, the IMAGE electrojet index IE from https://space.fmi.fi/image/, the SuperMAG electrojet indices SME and SML from https://supermag.jhuapl.edu/indices/?tab=download&layers=SME.UL&fidelity=low and the Polar Cap index PCN from https://ftp.space.dtu.dk/WDC/indices/pcn/. The data is publicly available and we like to thank the data providers for kindly sharing their data.

Appendix A. List of storm events 2011–2017

See Table 1.

Appendix B. List of correlation values

See Table 2.

Table 1
For the statistical analysis, the storm list used in Borries et al. (2009) has been complemented by the dates listed here. This sums up to a total number of 60 events.

Date	min. Dst (nT)
2011-09-26	−118
2011-10-25	−147
2012-03-09	−145
2012-04-24	−120
2012-07-15	−139
2012-10-01	−122
2013-03-17	−132
2013-06-01	−124
2014-02-19	−119
2015-01-07	−107
2015-03-17	−234
2015-06-23	−204
2015-10-07	−124
2015-11-03	−55
2015-12-20	−166
2016-04-02	−59
2016-10-13	−110
2017-03-01	−61
2017-03-27	−70
2017-05-28	−125
2017-07-16	−72
2017-08-31	−51
2017-09-08	−122
2017-09-14	−33
2017-11-07	−71

Table 2
Correlation coefficients of solar and geomagnetic parameters x with the maximum A_{TID} measured at the GNSS station GLSV. Each value reflects the Person correlation coefficient and in brackets its p-value. Correlation values for the non-linear functions (second and third column) are only presented for those cases, where the correlation improves compared to the linear correlation (first column).

Parameter x	$ax+b$	ax^2+b	$a\sqrt{e^x}+b$
max(AE)	0.72 (2.8e−10)	0.76 (6.9e−10)	
max(dAE/dt)	0.69 (3.3e−09)		
max(AU)	0.60 (4.2e−07)		
max(dAU/dt)	0.73 (1.1e−09)		
min(AL)	−0.70 (9.4e−10)		
min(dAL/dt)	−0.56 (3.1e−06)		
max(IE)	0.53 (1.3e−05)		
max(dIE/dt)	0.66 (7.4e−08)		
max(PCN)	0.70 (4.9e−10)		
max(dPCN/dt)	0.69 (1.0e−08)		
max(kp)	0.60 (5.2e−07)	0.65 (2.6e−08)	0.70 (5.0e−10)
max(dkp/dt)	0.15 (2.4e−01)		
max(ap)	0.71 (3.2e−10)		
max(dap/dt)	0.80 (7.7e−14)		
min(Dst)	−0.76 (7.1e−12)		
min(dDst/dt)	−0.78 (1.2e−12		
min(SYM-H)	−0.63 (1.6e−07)		
min(dSYM-H/dt)	−0.69 (3.9e−09)		
max(SME)	0.66 (7.3e−09)	0.68 (2.2e−9)	
max(dSME/dt)	0.57 (2.8e−06)		
min(SML)	−0.75 (9.1e−12)	0.79 (2.7e−13)	
min(Bz)	−0.76 (9.2e−12)	0.78 (1.2e−12)	
min(dBz/dt)	−0.67 (1.2e−08)		
max(E_{KL})	0.79 (3.2e−13)		
max(dE_{KL}/dt)	0.69 (2.8e−09)	0.73 (1.4e−10)	
max(E_{wav})	0.79 (8.6e−13)		
max(dE_{wav}/dt)	0.73 (3.1e−10)	0.77 (1.5e−11)	
max(E_{wv})	0.76 (5.5e−12)		
max(dE_{wv}/dt)	0.58 (2.8e−06)	0.60 (8.3e−07)	
max($\epsilon 3$)	0.80 (1.5e−13)		
max($d\epsilon 3/dt$)	0.70 (1.3e−09)		
max($d\Phi/dt$)	0.79 (7.4e−13)		
max(ddΦ/dtdt)	0.61 (6.2e−07)		

References

Adhikari, B., Dahal, S., Sapkota, N., Baruwal, P., Bhattarai, B., Khanal, K., Chapagain, N.P., 2018. Field-aligned current and polar cap potential and geomagnetic disturbances: A review of cross-correlation analysis. Earth Space Sci. 5 (9), 440–455. http://dx.doi.org/10.1029/2018ea000392.

Afraimovich, E., Voeykov, S., Perevalova, N., Ratovsky, K., 2008. Large-scale traveling ionospheric disturbances of auroral origin according to the data of the GPS network and ionosondes. Adv. Space Res. 42 (7), 1213–1217. http://dx.doi.org/10.1016/j.asr.2007.11.023.

Becker, E., Vadas, S.L., 2020. Explicit Global Simulation of Gravity Waves in the Thermosphere. J. Geophys. Res. Space Phys. 125 (10), http://dx.doi.org/10.1029/2020ja028034.

Belehaki, A., Tsagouri, I., Altadill, D., Blanch, E., Borries, C., Buresova, D., Chum, J., Galkin, I., Juan, J.M., Segarra, A., Timoté, C., Tziotziou, K., Verhulst, T., Watermann, J., 2020. An overview of methodologies for real-time detection, characterisation and tracking of Traveling Ionospheric Disturbances developed in the TechTIDE project. J. Space Weather Space Clim. 10 (42), http://dx.doi.org/10.1051/swsc/2020043.

Blanch, E., Altadill, D., Boška, J., Burešová, D., Hernández-Pajares, M., 2005. November 2003 event: effects on the Earth's ionosphere observed from ground-based ionosonde and GPS data. Ann. Geophys. 23, 3027–3034. http://dx.doi.org/10.5194/angeo-23-3027-2005, URL: https://angeo.copernicus.org/articles/23/3027/2005/.

Bloomfield, D.S., Higgins, P.A., McAteer, R.T.J., Gallagher, P.T., 2012. Toward Reliable Benchmarking of Solar Flare Forecasting Methods. Astrophys. J. 747 (2), L41. http://dx.doi.org/10.1088/2041-8205/747/2/l41.

Bobra, M.G., Couvidat, S., 2015. Solar flare prediction using SDO/HMI vector magnetic field data with a machine-learning algorithm. Astrophys. J. 798 (2), 135. http://dx.doi.org/10.1088/0004-637x/798/2/135.

Borries, C., Jakowski, N., Kauristie, K., Amm, O., Mielich, J., Kouba, D., 2017. On the dynamics of large-scale traveling ionospheric disturbances over Europe on 20 November 2003. J. Geophys. Res. Space Phys. 122 (1), 1199–1211. http://dx.doi.org/10.1002/2016JA023050, 2016JA023050.

Borries, C., Jakowski, N., Wilken, V., 2009. Storm induced large scale TIDs observed in GPS derived TEC. Ann. Geophys. 27 (4), 1605–1612. http://dx.doi.org/10.5194/angeo-27-1605-2009, URL: http://www.ann-geophys.net/27/1605/2009/.

Borries, C., Mahrous, A.M., Ellahouny, N.M., Badeke, R., 2016. Multiple ionospheric perturbations during the Saint Patrick's Day storm 2015 in the European-African sector. J. Geophys. Res. Space Phys. 121 (11), 11,333–11,345. http://dx.doi.org/10.1002/2016JA023178, 2016JA023178.

Camporeale, E., 2019. The Challenge of Machine Learning in Space Weather: Nowcasting and Forecasting. Space Weather 1166–1207. http://dx.doi.org/10.1029/2018SW002061, URL: https://agupubs.onlinelibrary.wiley.com/doi/full/10.1029/2018SW002061.

Cherniak, I., Zakharenkova, I., 2018. Large-scale traveling ionospheric disturbances origin and propagation: Case study of the december 2015 geomagnetic storm. Space Weather 16 (9), 1377–1395. http://dx.doi.org/10.1029/2018sw001869.

Chou, M.-Y., Pedatella, N.M., Wu, Q., Huba, J.D., Lin, C.C.H., Schreiner, W.S., Braun, J.J., Eastes, R.W., Yue, J., 2020. Observation and simulation of the development of equatorial plasma bubbles: Post-sunset rise or upwelling growth? J. Geophys. Res. Space Phys. 125 (12), 1–14. http://dx.doi.org/10.1029/2020JA028544.

Davis, T.N., Sugiura, M., 1966. Auroral electrojet activity index AE and its universal time variations. J. Geophys. Res. 71 (3), 785–801. http://dx.doi.org/10.1029/jz071i003p00785.

Detman, T., Joselyn, J., 1999. Real-time Kp predictions from ACE real time solar wind. AIP Conf. Proc. 471 (1), 729–732. http://dx.doi.org/10.1063/1.58720, arXiv:https://aip.scitation.org/doi/pdf/10.1063/1.58720 URL: https://aip.scitation.org/doi/abs/10.1063/1.58720.

Ding, F., Wan, W., Liu, L., Afraimovich, E., Voeykov, S., Perevalova, N., 2008. A statistical study of large-scale traveling ionospheric disturbances observed by GPS TEC during major magnetic storms over the years 2003–2005. J. Geophys. Res. Space Phys. 113 (A3), A00A01. http://dx.doi.org/10.1029/2008JA013037.

Ding, F., Wan, W., Ning, B., Wang, M., 2007. Large-scale traveling ionospheric disturbances observed by GPS total electron content during the magnetic storm of 29-30 October 2003. J. Geophys. Res. 112, A06309. http://dx.doi.org/10.1029/2006JA012013.

Eastes, R.W., Solomon, S.C., Daniell, R.E., Anderson, D.N., Burns, A.G., England, S.L., Martinis, C.R., McClintock, W.E., 2019. Global-scale observations of the equatorial ionization anomaly. Geophys. Res. Lett. 46 (16), 9318–9326. http://dx.doi.org/10.1029/2019GL084199.

Fedorenko, Y.P., Tyrnov, O.F., Fedorenko, V.N., Dorohov, V.L., 2013. Model of traveling ionospheric disturbances. J. Space Weather Space Clim. 3, A30. http://dx.doi.org/10.1051/swsc/2013052.

Habarulema, J.B., Katamzi, Z.T., Yizengaw, E., 2015. First observations of poleward large-scale traveling ionospheric disturbances over the African sector during geomagnetic storm conditions. J. Geophys. Res. Space Phys. http://dx.doi.org/10.1002/2015JA021066, 2015JA021066.

Hajkowicz, L., 1991. Auroral electrojet effect on the global occurrence pattern of large scale travelling ionospheric disturbances. Planet. Space Sci. 39 (8), 1189–1196. http://dx.doi.org/10.1016/0032-0633(91)90170-f.

Hernández-Pajares, M., Juan, J.M., Sanz, J., 2006. Medium-scale traveling ionospheric disturbances affecting GPS measurements: Spatial and temporal analysis. J. Geophys. Res. Space Phys. 111 (A7), http://dx.doi.org/10.1029/2005JA011474, URL: https://agupubs.onlinelibrary.wiley.com/doi/abs/10.1029/2005JA011474.

Hocke, K., Schlegel, K., 1996. A review of atmospheric gravity waves and travelling ionospheric disturbances: 1982–1995. Ann. Geophys. 14 (9), 917–940, URL: http://www.ann-geophys.net/14/917/1996/.

Hofmann-Wellenhof, B., Lichtenegger, H., Collins, J., 2012. Global Positioning System: Theory and Practice. Springer Vienna, URL: https://books.google.de/books?id=F7jrCAAAQBAJ.

Hunsucker, R.D., 1982. Atmospheric Gravity Waves Generated in the High-Latitude Ionosphere: A Review. Rev. Geophys. Space Phys. 20 (2), 293–315.

Iijima, T., Potemra, T.A., 1982. The relationship between interplanetary quantities and Birkeland current densities. Geophys. Res. Lett. 9 (4), 442–445. http://dx.doi.org/10.1029/gl009i004p00442.

Kahler, S.W., Darsey, H., 2021. Exploring contingency skill scores based on event sizes. Space Weather 19 (5), http://dx.doi.org/10.1029/2020sw002604.

van de Kamp, M., Pokhotelov, D., Kauristie, K., 2014. TID characterised using joint effort of incoherent scatter radar and GPS. Ann. Geophys. 32 (12), 1511–1532. http://dx.doi.org/10.5194/angeo-32-1511-2014, URL: https://angeo.copernicus.org/articles/32/1511/2014/.

Korth, H., Anderson, B.J., Waters, C.L., 2010. Statistical analysis of the dependence of large-scale Birkeland currents on solar wind parameters. Ann. Geophys. 28 (2), 515–530. http://dx.doi.org/10.5194/angeo-28-515-2010.

Krall, J., Huba, J.D., Ossakow, S.L., Joyce, G., Makela, J.J., Miller, E.S., Kelley, M.C., 2011. Modeling of equatorial plasma bubbles triggered by non-equatorial traveling ionospheric disturbances. Geophys. Res. Lett. 38 (8), n/a. http://dx.doi.org/10.1029/2011gl046890.

Liu, J., Zhang, D.-H., Coster, A.J., Zhang, S.-R., Ma, G.-Y., Hao, Y.-Q., Xiao, Z., 2019a. A case study of the large-scale traveling ionospheric disturbances in the eastern Asian sector during the 2015 St. Patrick's Day geomagnetic storm. Ann. Geophys. 37 (4), 673–687. http://dx.doi.org/10.5194/angeo-37-673-2019, URL: https://angeo.copernicus.org/articles/37/673/2019/.

Liu, Y., Zhou, C., Tang, Q., Kong, J., Gu, X., Ni, B., Yao, Y., Zhao, Z., 2019b. Evidence of mid- and low-latitude nighttime ionospheric $E - F$ coupling: Coordinated observations of sporadic E layers, F -region field-aligned irregularities, and medium-scale traveling ionospheric disturbances. IEEE Trans. Geosci. Remote Sens. 57 (10), 7547–7557. http://dx.doi.org/10.1109/TGRS.2019.2914059.

Lu, G., Zakharenkova, I., Cherniak, I., Dang, T., 2020. Large-scale ionospheric disturbances during the 17 march 2015 storm: A model-data comparative study. J. Geophys. Res. Space Phys. 125 (5), http://dx.doi.org/10.1029/2019ja027726.

Lyons, L.R., Nishimura, Y., Zhang, S.-R., Coster, A.J., Bhatt, A., Kendall, E., Deng, Y., 2019. Identification of auroral zone activity driving large-scale traveling ionospheric disturbances. J. Geophys. Res. Space Phys. 124 (1), 700–714. http://dx.doi.org/10.1029/2018ja025980.

Mukhopadhyay, A., Welling, D.T., Liemohn, M.W., Ridley, A.J., Chakraborty, S., Anderson, B.J., 2020. Conductance model for extreme events: Impact of auroral conductance on space weather forecasts. Space Weather 18 (11), http://dx.doi.org/10.1029/2020sw002551.

Negale, M.R., Taylor, M.J., Nicolls, M.J., Vadas, S.L., Nielsen, K., Heinselman, C.J., 2018. Seasonal Propagation Characteristics of MSTIDs Observed at High Latitudes Over Central Alaska Using the Poker Flat Incoherent Scatter Radar. J. Geophys. Res. Space Phys. 123 (7), 5717–5737. http://dx.doi.org/10.1029/2017ja024876.

Newell, P.T., Gjerloev, J.W., 2011. Evaluation of SuperMAG auroral electrojet indices as indicators of substorms and auroral power. J. Geophys. Res. Space Phys. 116 (A12), http://dx.doi.org/10.1029/2011ja016779.

Newell, P.T., Sotirelis, T., Liou, K., Meng, C.-I., Rich, F.J., 2007. A nearly universal solar wind-magnetosphere coupling function inferred from 10 magnetospheric state variables. J. Geophys. Res. Space Phys. 112 (A1), n/a. http://dx.doi.org/10.1029/2006ja012015.

Nykiel, G., Zanimonskiy, Y., Koloskov, A., Figurski, M., 2019. The possibility of estimating the height of the ionospheric inhomogeneities based on TEC variations maps obtained from dense GPS network. Adv. Space Res. 64 (10), 2002–2011. http://dx.doi.org/10.1016/j.asr.2019.06.008.

Prölss, G.W., 2006. Ionospheric F-region Storms: Unsolved Problems. In: Characterising the Ionosphere. 10–1–10–20, URL: http://ftp.rta.nato.int/public//PubFullText/RTO/MP/RTO-MP-IST-056///MP-IST-056-10.pdf.

Reikard, G., 2018. Forecasting space weather over short horizons: Revised and updated estimates. New Astron. 62–69. http://dx.doi.org/10.1016/j.newast.2018.01.009, URL: https://www.sciencedirect.com/science/article/abs/pii/S1384107617303895?via%3Dihub.

Saito, A., Fukao, S., Miyazaki, S., 1998. High resolution mapping of TEC perturbations with the GSI GPS network over Japan. Geophys. Res. Lett. 25, 3079–3082. http://dx.doi.org/10.1029/98GL52361.

Saito, S., Yamamoto, M., Hashiguchi, H., Maegawa, A., Saito, A., 2007. Observational evidence of coupling between quasi-periodic echoesand medium scale traveling ionospheric disturbances. Ann. Geophys. 25, 2185–2194, URL: http://www.ann-geophys.net/25/2185/2007/angeo-25-2185-2007.pdf.

Shiokawa, K., Otsuka, Y., Ogawa, T., Balan, N., Igarashi, K., Ridley, A., Knipp, D., Saito, A., Yumoto, K., 2002. A large-scale traveling ionospheric disturbance during the magnetic storm of 15 September 1999. J. Geophys. Res. 107 (A6), 1088. http://dx.doi.org/10.1029/2001JA000245.

Singh, S., Johnson, F.S., Power, R.A., 1997. Gravity wave seeding of equatorial plasma bubbles. J. Geophys. Res. Space Phys. 102 (A4), 7399–7410. http://dx.doi.org/10.1029/96ja03998.

Singh, A.K., Sinha, A., Saini, S., Rawat, R., 2015. Auroral electrojets during severely disturbed geomagnetic condition on 24 August 2005. Adv. Space Res. 55 (5), 1349–1355. http://dx.doi.org/10.1016/j.asr.2014.11.034.

Sivakandan, M., Martinis, C., Otsuka, Y., Chau, J.L., Norrell, J., Mielich, J., Conte, J.F., Stolle, C., Rodríguez-Zuluaga, J., Shinbori, A., Nishioka, M., Tsugawa, T., 2022. On the role of E-F region coupling in the generation of nighttime MSTIDs during summer and equinox: Case studies over Northern Germany. J. Geophys. Res. Space Phys. 127 (5), 1–19. http://dx.doi.org/10.1029/2021JA030159.

Song, Q., Ding, F., Wan, W., Ning, B., Liu, L., Zhao, B., Li, Q., Zhang, R., 2013. Statistical study of large-scale traveling ionospheric disturbances generated by the solar terminator over China. J. Geophys. Res. Space Phys. 118 (7), 4583–4593. http://dx.doi.org/10.1002/jgra.50423, arXiv:https://agupubs.onlinelibrary.wiley.com/doi/pdf/10.1002/jgra.50423 URL: https://agupubs.onlinelibrary.wiley.com/doi/abs/10.1002/jgra.50423.

Thaganyana, G.P., Habarulema, J.B., Ngwira, C., Azeem, I., 2022. Equatorward medium to large-scale traveling ionospheric disturbances of high latitude origin during quiet conditions. J. Geophys. Res. Space Phys. 127 (3), http://dx.doi.org/10.1029/2021ja029558.

Tsugawa, T., Kotake, N., Otsuka, Y., Saito, A., 2007. Medium-scale traveling ionospheric disturbances observed by GPS receiver network in Japan: a short review. GPS Solut. 11, 139–144. http://dx.doi.org/10.1007/s10291-006-0045-5, URL: http://www.springerlink.com/content/u2g42vj57h70g042/fulltext.pdf.

Tsugawa, T., Saito, A., Otsuka, Y., 2004. A statistical study of large-scale travelling ionospheric disturbances using the GPS network in Japan. J. Geophys. Res. 109 (A06302), 1–11.

Tsunoda, R.T., White, B.R., 1981. On the generation and growth of equatorial backscatter plumes 1. Wave structure in the bottomside F layer. J. Geophys. Res. 86 (A5), 3610. http://dx.doi.org/10.1029/ja086ia05p03610.

Verkhoglyadova, O., Meng, X., Mannucci, A.J., Shim, J.-S., McGranaghan, R., 2020. Evaluation of total electron content prediction using three ionosphere-thermosphere models. Space Weather 18 (9), http://dx.doi.org/10.1029/2020sw002452.

Vlasov, A., Kauristie, K., van de Kamp, M., Luntama, J.-P., Pogoreltsev, A., 2011. A study of Traveling Ionospheric Disturbances and Atmospheric Gravity Waves using EISCAT Svalbard Radar IPY-data. Ann. Geophys. 29 (11), 2101–2116. http://dx.doi.org/10.5194/angeo-29-2101-2011, URL: http://www.ann-geophys.net/29/2101/2011/.

Welling, D.T., Ngwira, C.M., Opgenoorth, H., Haiducek, J.D., Savani, N.P., Morley, S.K., Cid, C., Weigel, R., Weygand, J.M., Woodroffe, J.R., Singer, H., Rosenqvist, L., Liemohn, M., 2018. Recommendations for next-generation ground magnetic perturbation validation. Space Weather 16 (12), 1912–1920. http://dx.doi.org/10.1029/2018sw002064.

Zakharenkova, I., Astafyeva, E., Cherniak, I., 2016. GPS & GLONASS observations of large-scale traveling ionospheric disturbances during the 2015 St. Patrick's Day storm. J. Geophys. Res. Space Phys. n/a–n/a. http://dx.doi.org/10.1002/2016JA023332, 2016JA023332.

Zhang, S.R., Erickson, P.J., Coster, A.J., Rideout, W., Vierinen, J., Jonah, O., P.Goncharenko, L., 2019. Subauroral and polar traveling ionospheric disturbances during the 7–9 September 2017 storms. Space Weather 17 (12), 1748–1764. http://dx.doi.org/10.1029/2019sw002325.

Zhang, J., Richardson, G., Webb, D.F., Gopalswamy, N., Huttunen, E., Kasper, J.C., Nitta, N.V., Poomvises, W., Thompson, B.J., Wu, C.-C., Yashiro, S., Zhukov, A.N., 2007. Solar and interplanetary sources of major geomagnetic storms (Dst $\leq$ -100 nT) during 1996–2005. J. Geophys. Res. 1–19. http://dx.doi.org/10.1029/2007JA012321, URL: https://agupubs.onlinelibrary.wiley.com/doi/full/10.1029/2007JA012321.